

# HARTII: Experimental Analysis and Validation of ONERA Methodology for the Prediction of Blade-Vortex Interaction

Joëlle BAILLY, Yves DELRIEUX, Philippe BEAUMIER  
Office National d'Etudes et de Recherches Aéronautiques, ONERA  
Châtillon, France

## Abstract

In 1994 and 2001, two experimental campaigns, called HART and HART II, were conducted in the DNW German-Dutch wind tunnel, in the framework of the US-German and US-French Memoranda of Understanding, in cooperation between NASA Langley, US Army Aeroflightdynamics Directorate (AFDD), DLR, DNW and ONERA. The experimental program was conducted with a BO105 main rotor model. The objective of these campaigns was to study the effects of the Higher Harmonic pitch Control on the blade vortex interactions (responsible for BVI noise and high vibration levels). Different measurements were performed, such as blade pressure distributions, blade airloads, acoustic measurements, blade deformations, wake geometry, and velocity field. The HART II campaign extended the HART data with new measurements techniques, more especially the 3-components PIV technique for the wake measurements, performed jointly by the DNW and DLR teams.

The first part of the paper concerns the post-processing of PIV data performed at ONERA, which in first consists in analysing the flowfield and determining the locations of the vortex centres, and in a second step, in determining the vortex parameters. Then, in a second part, the validation of the different steps of the ONERA aero-acoustic computational chain is presented, showing satisfactory correlations with experiment.

## Notations

### Abbreviations

|      |   |
|------|---|
| BL   | Baseline  |
| HART | Higher harmonic control Aeroacoustic Rotor Test |
| CW   | Clockwise                                       |
| CCW  | Counter-Clockwise                               |
| HHC  | Higher Harmonic Control                         |
| MN   | Minimum Noise                                   |
| MV   | Minimum Vibration                               |
| PIV  | Particle Image Velocimetry                      |
| SPR  | Stereo Pattern Recognition                      |

### Symbols

|   |                           |
|---|---------------------------|
| M | Mach number               |
| R | rotor radius, 2m          |
| c | rotor blade chord, 0.121m |

|                 |   |
|-----------------|---|
| $(x,y,z)_{PIV}$ | PIV coordinate system (x positive downstream, y positive up, z positive towards the observer) |
| $(x,y,z)_{HUB}$ | HUB coordinate system (x positive downstream, y normal to x, z positive up)                   |
| $(u,v,w)$       | velocity components in $(x,y,z)$ in PIV frame (m/s)   |
| $\omega_z$      | vorticity normal to $(x,y)$ plane in PIV frame, $s^{-1}$                                      |
| $r_c$           | vortex core radius, m   |
| $\Gamma_c$      | circulation at $r_c$ , $m^2/s$  |
| $V_c$           | swirl velocity at $r_c$ , m/s   |
| n               | parameter associated with analytical velocity profile   |
| $\Psi$          | azimuth angle, deg ( $0^\circ$ aft)   |
| $\theta$        | collective pitch angle, deg   |
| $\theta_{1c}$   | longitudinal pitch angle, deg   |
| $\theta_{1s}$   | lateral pitch angle, deg  |
| $C_n$           | sectional normal force coefficient  |

## Introduction

The amount of noise radiated from a helicopter rotor has always affected the use of rotorcrafts, especially in urban environment. The noise sources depend on the flight configurations. In particular, BVI noise generated by the interaction between the blades and the wake mainly occurs during descent flight, and is particularly penalizing. During the two last decades, significant efforts have been undertaken to improve the understanding and the prediction of BVI noise, in view of its reduction, thanks on the one hand to well-documented experimental tests, and on the other hand, to development and improvement of aero-acoustic codes.

In particular, a significant database was obtained in 1994 during the HART campaign (Refs. 1, 2), and in 2001 during the HART II campaign (Refs. 3-5). This program was performed in the framework of an international cooperation between NASA Langley, US Army, DLR, DNW, and ONERA. This database contains information on different topics, such as aerodynamics (blade pressure, vortex positions, velocity fields), dynamics (elastic deformations, Ref. 6), and acoustics, concerning the BO105 model rotor, trimmed with different control laws. Significant progress in aeroacoustic analysis and validations were performed to understand the effects of HHC on reduction of noise levels and vibration (Refs. 7-11). Furthermore, the HART II

campaign complemented the HART data with new measurement techniques, more especially the 3-components PIV technique for the wake measurements, performed jointly by DLR and DNW (Ref. 12)

In this paper, the post-processing of the PIV data, performed at ONERA, is presented, which consists in analyzing the flowfield and determining the vortex parameters. Then, in a second part, the ONERA aero-acoustic computational chain is validated by comparison with the experimental data (Ref. 13).

### **Rotor Model Description and Test Setup**

The HART II program was conducted in the open-jet, anechoic configuration of 8m x 6m cross-section of the DNW. The set-up for the PIV measurement is shown in Fig. 1. The rotor hub was maintained at 915mm above the longitudinal centreline, which corresponds to a noise measurement plane 2.215m below the hub centre. The longitudinal and lateral positions of the hub centre were 0.05m downstream and 0m from the tunnel centre.



Figure 1: HART hingeless model rotor in the DNW wind tunnel.

The HART II tests were performed on a 40% Mach scaled BO105 main rotor model, 4m in diameter, equipped with four hingeless blades, which have a pre-cone angle of 2.5°. The blades are rectangular, with -8°/R of linear twist, and they are equipped with modified NACA23012 airfoil, with a chord length of 0.121m.

The nominal rotor operating speed was 1041rpm, corresponding to a tip Mach number of 0.641. The tunnel speed was 33m/sec, which corresponds to an advance ratio of 0.15. The thrust coefficient  $C_T$  was equal to 0.0044, which corresponds to a moderate loading. Different shaft angles were chosen in the test plan, from climb to descent configurations. In this paper, three test configurations, one with no HHC (Baseline or BL), two with HHC (Minimum

Noise or MN and Minimum Vibration or MV), for the shaft angle of 5.3°, will be presented.

### **Three-Component PIV measurements**

The rotor wake was measured on both the advancing and retreating sides of the blades, when the reference blade is located at  $\Psi=20^\circ$ , then at  $\Psi=70^\circ$ , using a 3-C PIV technique. These measurements were performed on 53 locations on the rotor disk, shown in Fig. 2 for the Minimum Noise configuration. Each cut plane is oriented approximately 30.7° from the tunnel axis. The frames are in rows such that the y-axis cuts through the same yhub axis value. The different cut planes are located at  $y_{hub}=\pm 0.8, \pm 1.1, \pm 1.4, \pm 1.7, \pm 1.94\text{m}$ , respectively on the advancing and retreating sides.

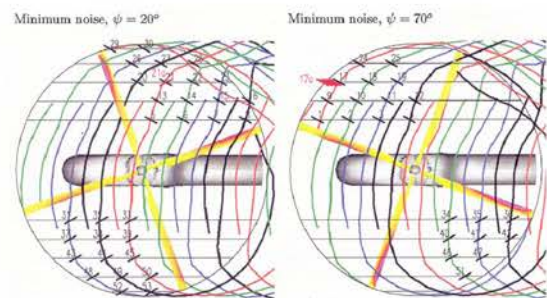


Figure 2: Locations of PIV cut planes, for the MN configuration.

For each location, 100 instantaneous PIV data (containing the coordinates of the PIV windows, and the three components of the velocity field) were recorded. For the high majority of the data points, the PIV data were obtained from two systems, to have complementary information on the wake. The first system operated by DNW consists in having a large image of the vortex and its surrounding flowfield. The DNW data were obtained over a nominally 43.5cm x 36.7cm frame, with a 32x32 pixels interrogation window size. The PIV measurements performed by DLR focussed on the vortex core region, on a 15.2cm x 12.9cm frame, centred within the large DNW windows. Different interrogation window sizes were used (32x32, 24x24, 20 x 20 and 16 x 16 pixels).

The centre of the PIV window was located in the wind tunnel coordinate system, as well as the location of the centre of rotation of the rotor. These coordinates are useful to localise the vortices in the wind tunnel, and then in the hub coordinate systems, in order to be compared with theoretical results.

### **PIV Post-Processing**

The first objective of the post-processing of PIV data is the determination of the location of the vortex centres, in the PIV coordinate system, then

in the hub coordinate system, which is well adapted for the comparison with numerical predictions. The different steps of the ONERA methodology are now described.

#### Simple Average

For each discretized point  $(i,j)$  of a PIV window, containing  $N_i$  points in the horizontal direction, and  $N_j$  points in the vertical direction, the simple average consists in computing the averaged velocity field  $(\bar{u}, \bar{v})$  from the 100 instantaneous velocity fields  $(u_i, v_i)$ , such as:

$$(\bar{u}(i, j), \bar{v}(i, j)) = \frac{1}{100} \sum_{n=1}^{100} (u_i(i, j), v_i(i, j))$$

for  $i$  varying from 1 to  $N_i$ ,  $j$  from 1 to  $N_j$ .

Then, the normal component of the averaged vorticity field can be calculated as:

$$\omega_z = (\overrightarrow{rotV})k = \frac{\partial \bar{v}}{\partial x} - \frac{\partial \bar{u}}{\partial y}$$

and discretized by a classical centred difference scheme, of second order in space, defined as:

$$\omega_z(i, j) = \frac{\bar{v}(i+1, j) - \bar{v}(i-1, j)}{2\Delta x} - \frac{\bar{u}(i, j+1) - \bar{u}(i, j-1)}{2\Delta y}$$

for  $i$  varying from 2 to  $N_i-1$ ,  $j$  from 2 to  $N_j-1$ , where  $\Delta x$  and  $\Delta y$  represent the grid spacing of the PIV window in the two directions. In order to avoid unrealistic value of discretized vorticity at the boundaries, the averaged vorticity field is not calculated at the edges of the PIV windows.

**Flowfield Analysis.** Fig. 3 shows the simple averaged vorticity field, at Position 19 for the Baseline and MN cases, and at Position 18 for the MV case, in the large DNW frames. These positions correspond to the last location of the PIV cut plane, in the second quadrant of the rotor disk (reference blade at  $\Psi=70^\circ$ , advancing side), and the coordinates in the hub system are defined as  $-230 \text{ mm} \leq x_{\text{hub}} \leq -87 \text{ mm}$ , and  $y_{\text{hub}} = 1.4 \text{ m}$ . For the Baseline and the MN configurations, the shear layer which rolls up at its end by the counter clockwise tip vortex can be easily distinguished. Furthermore, the trace of the wake generated by the preceding blades is easily identified. For the MV configuration, the structures of two counter-rotating vortices are clearly visible. It has been shown that this system of vortices can be related to a negative loading around  $130^\circ$  (azimuth where the emission of vortices responsible for BVI noise occurs). The first vortex (in blue) has a negative intensity of vorticity, which corresponds to the clockwise (CW) tip vortex. It is located above the vortex of positive intensity (in red), which corresponds to the counter-clockwise (CCW) inboard vortex. One can notice that the influence of the pitch control law is very important on the flowfield (generation of tip

vortices with different intensity, different convection of the vortex sheets).

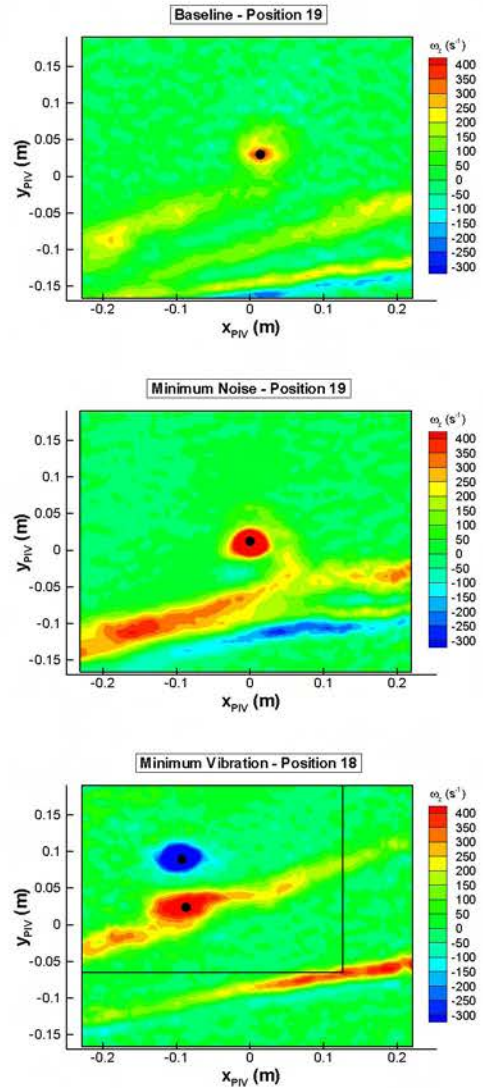


Figure 3: Simple averaged vorticity field, for the BL, MN, and MV configurations.

Table 1 gives the values of the maximum vorticity for the CCW tip vortex for the BL and MN cases, for the CCW inboard vortex for the MV case, as well as the minimum vorticity for the CW tip vortex for the MV configuration. One can notice that the maximum of vorticity is higher for the MN than for the BL case. This can be linked with a higher value of loading for the MN than for the BL, around the azimuth of  $130^\circ$  where the vortices are emitted. This difference is a major effect of the high harmonic pitch control. For the MV case, the value of the intensity of vorticity of the CW tip vortex is quite important in comparison with the CCW inboard vortex.

| Configuration           | $(\omega_z)_{\max/\min}$ ( $s^{-1}$ ) |
|-------------------------|---------------------------------------|
| BL                      | 389                                   |
| MN                      | 1348                                  |
| MV - CCW inboard vortex | 505                                   |
| MV - CW tip vortex      | -1133                                 |

Table 1: Values of extrema intensity of simple averaged vorticity.

**Vortex centres.** The location of the centre of the vortex can be identified as the location of the maximum (or minimum) value of the vorticity. Nevertheless, it is mandatory to check that this position is detected in the vortex structure, and not in the vortex sheet, which can happen when the influence of the shear layer is not negligible with respect to the vortex. In that case, an adequate size of the PIV window has to be chosen to correctly detect the vortex centre. When necessary, the trace of the reduced window where the extremum value of the vorticity is detected is plotted in black, as in Figure 3.

#### Instantaneous PIV data

For each data point, 100 instantaneous velocity fields ( $u_i, v_i$ ) are known in the  $(x, y)$  PIV frame. The instantaneous vorticity in the normal direction of the frame can be calculated as:

$$\omega_z = (\text{rot} \vec{V})_z = \partial v_i / \partial x - \partial u_i / \partial y$$

and discretised by a classical centred difference scheme as:

$$\omega_z = \frac{v_i(i+1, j) - v_i(i-1, j)}{2\Delta x} - \frac{u_i(i, j+1) - u_i(i, j-1)}{2\Delta y}$$

for  $i$  varying from 2 to  $N_i-1$ ,  $j$  from 2 to  $N_j-1$ .

**Flowfield Analysis.** Fig. 4 shows instantaneous vorticity fields, for Sample 10, at Position 19 for the Baseline and MN configurations, and at Position 18 for the MV configuration, in the large DNW windows. It can be obviously noted that high levels of background noise cannot allow a clear analysis of the flowfield.

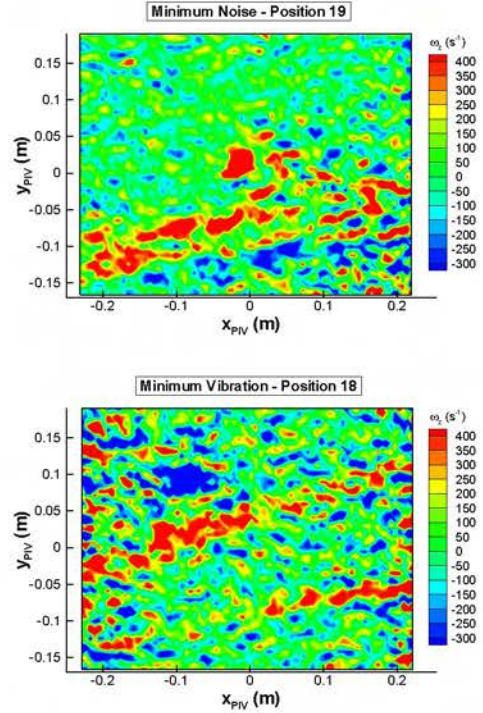
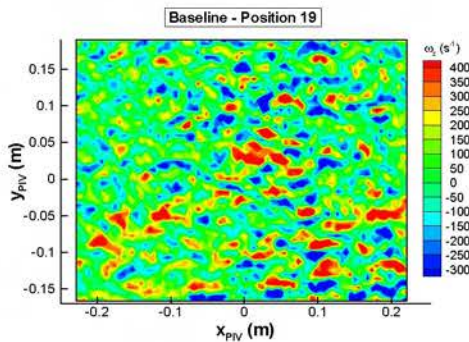


Figure 4: Instantaneous (Sample 10) vorticity field, at Position 19 for BL and MN, at Position 18 for MV.

**Vortex centres.** The vortex centres of all the instantaneous data are determined using the criterion based on the extremum value of vorticity, along one trajectory located at  $y_{\text{hub}}/R=0.7$ , on the advancing side of the blade, on the small and reduced DLR windows with the  $24 \times 24$  pixels resolution for the Baseline and Minimum Noise configurations, and on the large DNW windows for the Minimum Vibration configuration. Fig. 5 shows the evolutions of the locations of the instantaneous (symbols) and averaged (black line) vortex centres in the hub coordinate system, for the three configurations.

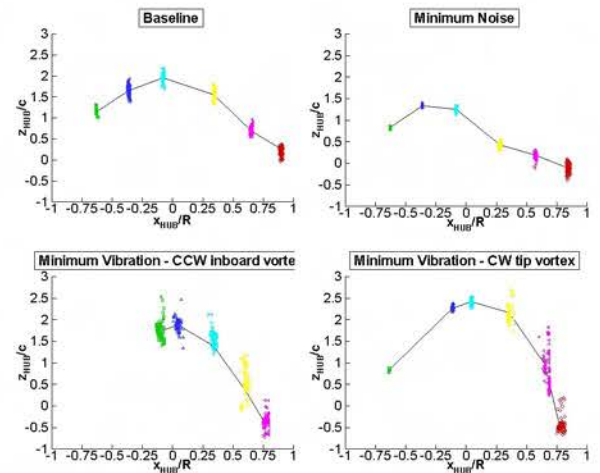


Figure 5: Vortex centre locations in the hub coordinate system, for the BL, MN and MV configurations.

First of all, one can notice, for the three configurations, that the vortex is convected upwards upstream of the rotor axis, and then is convected downwards, as expected. The positions of the instantaneous vortex centres illustrate the unsteady characteristic of the wake geometry. For the first position corresponding to the creation of the vortex, the instantaneous data are rather well concentrated around the vortex centre. The dispersion of these points is rather small (25% of chord for BL, 7% for MN, 10% for the CW tip vortex of the MV). Then, when the age of the vortices grows, the locations of the vortex centres are more scattered (around 50% of chord for BL, from 13 to 40% for MN, from 20 to 150% for the CW tip vortex of MV). It can be noticed that the locations of the instantaneous centres of the CCW inboard vortex of MV are particularly scattered. Such dispersion does not only reflect the unsteadiness of the vortex, but also the uncertainty of the evaluation of the vortex centre based on the location of extremum values of vorticity.

$\lambda_2$ -criterion. An other criterion, developed in the ONERA post-processing, can also be applied to distinguish the shear layers from the “hidden” vortex structures. It is based on the invariance of the tensor of the velocity gradient (Ref. 14). It can be shown that, in 2D approximation, for the velocity field defined by  $\vec{V} = (u(x, y), v(x, y))$ , a vortex is characterized by  $q > 0$  and  $\Delta < 0$ , where:

$$q = \det(\overrightarrow{\text{grad}}V) = \frac{\partial u}{\partial x} \frac{\partial v}{\partial y} - \frac{\partial v}{\partial x} \frac{\partial u}{\partial y}$$

$$p = \text{tr}(\overrightarrow{\text{grad}}V) = \frac{\partial u}{\partial x} + \frac{\partial v}{\partial y} \quad \text{Eq.(1)}$$

$\Delta = p^2 - 4q$   
This criterion is applied on Datapoint 862, corresponding to Position 22 of the Minimum Vibration configuration.

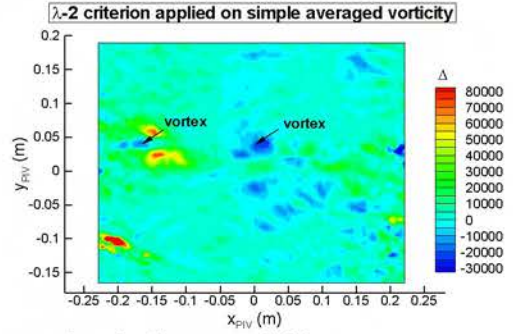
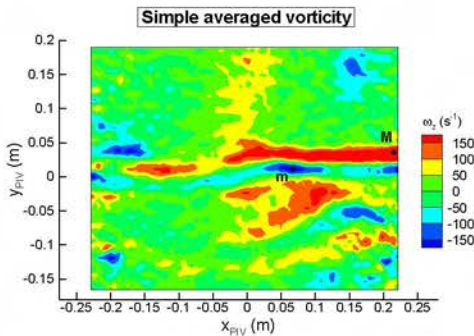


Figure 6: Application of  $\lambda_2$ -criterion on simple averaged vorticity, at Position 22 of MV configuration.

Fig. 6 shows that two vortex sheets (one with positive intensity in red, the second with negative intensity in blue) are predominant in the flowfield. The locations of the centres of the CCW and CW vortices determined by the maximum and minimum values of averaged vorticity are clearly in the vortex sheets. The application of the  $\lambda_2$ -criterion allows detecting two counter-rotating vortices (without information on the sense of rotation), thanks to concentrated areas where the value of the invariant  $\Delta$  is negative.

#### Rotational Component of Velocity

An innovative development in the ONERA post-processing is the analytical determination of the rotational component of the velocity field.

A general velocity field can be decomposed in two terms, the irrotational and the rotational components. Determining the rotational part of the velocity allows obtaining a better viewing of the rolling up of the velocity around a vortex structure. Up to now (Refs. 7, 8), the irrotational component was obtained by averaging the velocity on an arbitrary region which does not contain any vortex structure, and was subtracted from the total velocity field to obtain the rotational component of velocity.

The analytical procedure developed at ONERA consists in searching the rotational component of the velocity  $\vec{V}_{rot} = (u, v)$  which verifies the two relations (Ref. 15):

$$(a) \text{div}(\vec{V}_{rot}) = 0$$

$$(b) \text{rot}(\vec{V}_{rot}) = \vec{\omega} \quad \text{Eq. (2)}$$

$\vec{\omega}$  being the vorticity field determined in the PIV windows.

Eq. (2a) involves the existence of a stream function  $\Psi$  which verifies:

$$u = \frac{\partial \Psi}{\partial y}$$

$$v = -\frac{\partial \Psi}{\partial x} \quad \text{Eq. (3)}$$

By replacing these expressions in Eq. (2b), one obtains the Poisson equation  $\Delta\Psi = -\omega$ .

This equation can be solved by Green functions, and it is shown that in 2D dimensions (Ref. 15), the stream function which solves the Poisson equation is defined as:

$$\Psi(x, y) = \frac{1}{4\pi} \iint \omega_0 \ln[(x-x_0)^2 + (y-y_0)^2] dx_0 dy_0$$

where  $\omega_0$  is the value of the vorticity  $\omega_z$  at the point  $(x_0, y_0)$  describing the PIV frame.

The components  $(u, v)$  of the rotational part of the velocity are then easily calculated.

It is interesting to check that the vorticity computed with the rotational part of the velocity, calculated in that way, is similar to the vorticity field computed with the initial and total PIV velocity field. This is what is illustrated in Fig. 7, for the Position 22 of the Baseline Configuration (Datapoint 683).

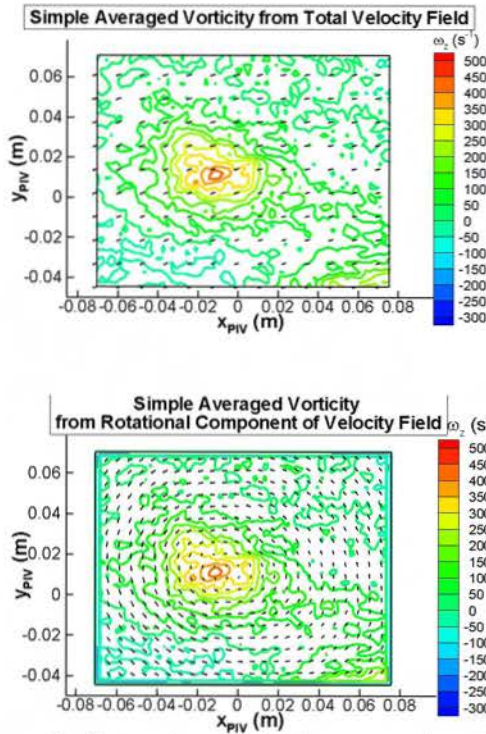


Figure 7: Comparison of simple averaged vorticity fields calculated from total velocity and rotational part of velocity, at Position 22, for the BL configuration.

One can already notice the rolling up, around the vortex structure, of the velocity vectors obtained with the rotational component. For clarity, only every fifth vector along a line is plotted in Figure 7. It is verified that the simple averaged vorticity fields computed from the total velocity field in one hand and from the rotational component of velocity on the other hand, are very similar. In the first case, the maximum value of vorticity is equal to  $489 \text{ s}^{-1}$  and to  $492 \text{ s}^{-1}$  in the second case. In the same way, the shape of the velocity profiles plotted along the vertical cut and the horizontal cut across the vortex

centre is very similar in the two cases (Fig. 8). A first estimation of the vortex parameters can be done, with the profiles of velocity across the vortex centres. The swirl velocity  $V_c$  can be approximated as the half of the difference of peak velocities, and the core radius  $r_c$  as the half of the distance between the locations of these peaks (Ref. 8). Table 2 gives the values of the vortex parameters obtained with the two approaches. One can notice that these values are very similar.

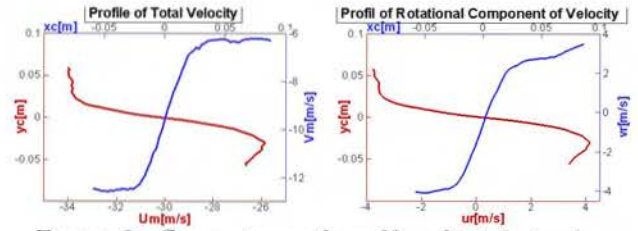


Figure 8: Comparison of profile of total simple averaged velocity and rotational part of simple averaged velocity, across the vortex centre, at Position 22, for the BL configuration.

| Method            | Total Velocity | Rot. Component |
|-------------------|----------------|----------------|
| uc (m/s)          | 4.00           | 3.84           |
| vc (m/s)          | 2.95           | 2.93           |
| xc ( $10^{-3}$ m) | 26.0           | 23.0           |
| yc ( $10^{-3}$ m) | 31.0           | 31.0           |

Table 2: Vortex parameters with simple average method.

This shows that this methodology gives a correct estimation of the rotational part of the velocity, without any arbitrary choice for the free stream velocity.

#### Conditional Average

The simple average method allows to analyze rather easily the evolution of the geometry of the wake (generation of tip vortices, interaction between vortices and shear layers), in a global way (with the removing of spurious background noise). But, this post-processing is not accurate enough to determine the vortex characteristics, such as velocity profiles, and vortex core size. The idea of the conditional average consists in first aligning the locations of the instantaneous vortex centres, prior to averaging (Ref. 8). In that way, the unsteady effects of the flowfield (vortex wandering) are removed.

More precisely, the computation of the conditional averaged vorticity is performed as follows in the ONERA methodology:

- Simple average of the 100 instantaneous PIV windows;
- Localization in the close region around the simple averaged vortex centre of the 100 instantaneous vortex centres;

- For each instantaneous map, shift at the point (0,0) the location of the instantaneous vortex centres;
- Determination of the smallest window containing all the shifted instantaneous maps, and calculation of the number of common windows;
- Computation of the averaged value of the velocity and vorticity fields on this smallest global window. This methodology is illustrated in Fig. 9, with the example of three PIV windows.

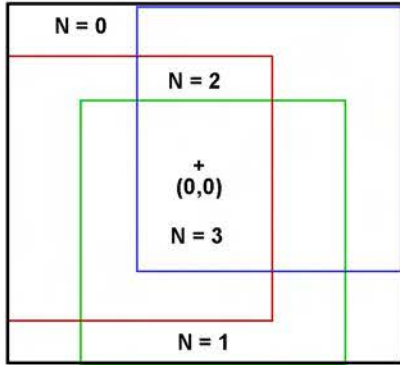


Figure 9: Determination of the envelop of three shifted instantaneous PIV windows.

In order to avoid locations of the extremum vorticities in the vortex sheets, it is recommended to perform this study on the small DLR windows, which are located close around the vortex centres. The conditional average tends to concentrate the vortex structure (Fig. 10) compared to the simple averaging (Fig. 7). Furthermore, the maximum values of vorticity at the centres of the vortex are very similar with the two approaches (total velocity and rotational component of velocity):  $2330 \text{ s}^{-1}$  with the total velocity and  $2244 \text{ s}^{-1}$  with the rotational component of velocity, which represents about 4.5 times the values of the maximum simple averaged vorticities.

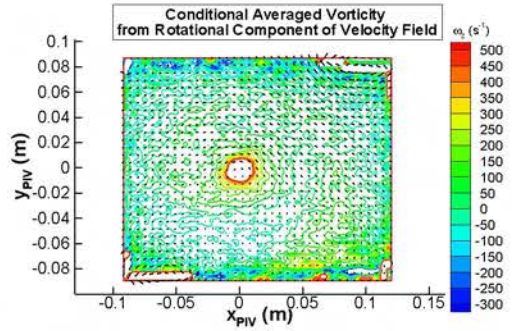
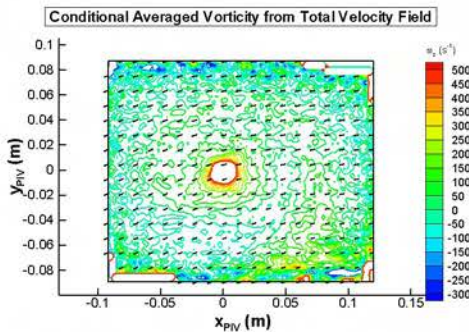


Figure 10: Comparison of conditional averaged vorticity fields calculated from total velocity and rotational part of velocity, at Position 22, for the BL configuration.

Moreover, the conditional average improves the sharpness of the velocity profiles (Fig. 11). Table 3 summarizes the values of the vortex parameters obtained from the velocity profiles. One can notice, once more, that both approaches (total velocity and rotational component of velocity) give very similar results. Furthermore, the conditional average method provides larger and more accurate swirl velocities and smaller core radii than the simple average method, as expected.

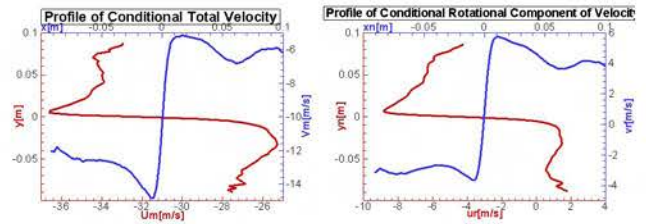


Figure 11: Comparison of profile of total conditional averaged velocity and rotational part of conditional averaged velocity, across the vortex centre, at Position 22, for the BL configuration.

| Method            | Total Velocity | Rot. Component |
|-------------------|----------------|----------------|
| uc (m/s)          | 5.42           | 5.04           |
| vc (m/s)          | 4.75           | 4.70           |
| xc ( $10^{-3}$ m) | 8.23           | 9.41           |
| yc ( $10^{-3}$ m) | 10.59          | 10.00          |

Table 3: Vortex parameters with conditional average method.

Finally, the number of common PIV windows calculated on the smallest global window is an important parameter, and will give qualitative information on the accuracy of the vortex parameters, which will be presented in the next paragraph.

**Flowfield Analysis.** The vorticity contours obtained by conditional average, at Position 19 for the Baseline and Minimum Noise cases, and at Position 18 for the Minimum Vibration configuration are plotted in Fig. 12. For the BL, MN and the MV CCW vortex, the conditional average is performed

around the maximum of vorticity. For the MV CW tip vortex, it is performed around the minimum value of vorticity. Fig. 12 clearly shows a much more concentrated vortex than with the simple average method, which tends to smooth the vorticity fields.

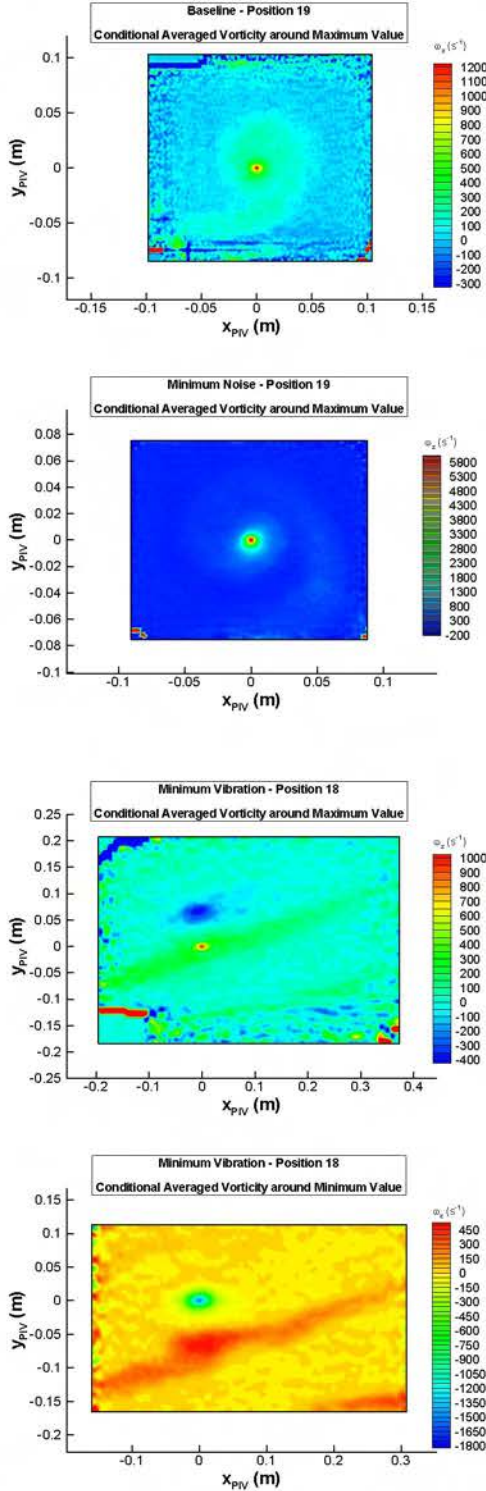


Figure 12: Conditional averaged vorticity field, at Position 19, for BL and MN, at Position 18 for MV.

Table 4 gives the values of the extremum intensity of conditional averaged vorticities. These

intensities are from 1.4 up to 5 times higher than those obtained with the simple average method (Table 1).

| Configuration           | $(\omega_z)_{\text{extremum}} \text{ (s}^{-1}\text{)}$ |
|-------------------------|--|
| BL                      | 1443   |
| MN                      | 6882   |
| MV - CCW inboard vortex | 1003   |
| MV - CW tip vortex      | -1557  |

Table 4: Values of extremum intensity of conditional averaged vorticity.

**Vortex parameters.** The second objective of the post-processing of the PIV data is the determination of the vortex parameters (circulation and swirl velocity distributions, vortex core size). These parameters are obtained with a better accuracy from the conditional averaged rotational component of the velocity fields. The “vorticity disk” integration method is applied to determine the vortex parameters (Ref. 8). It consists in integrating velocity over circles with increasing values of radius  $r$ , and centred at the point  $(0;0)$  of the conditional averaged window. The circulation  $\Gamma = \oint \vec{V} \cdot d\vec{l}$ , and the swirl velocity  $V_c = \Gamma / 2\pi r$  distributions are calculated as function of the radius  $r$ . The core size of the vortex corresponds to the radius where the maximum value of swirl velocity is obtained.

This methodology is applied to study the evolution of the characteristics of the tip vortex, generated along the trajectory located at  $y_{\text{hub}}/R=0.7$ , on the advancing side of the blade, for the Minimum Noise configuration (Fig. 2).

The analysis of the simple averaged vorticity field in the large DNW PIV windows reveals the generation of a well-defined shear layer, which rolls up at its end by a CCW vortex (Position 17). Then, as far as the age of the vortex grows (from Position 18 to Position 20), interactions between the shear layers of the preceding blades are visible, but the structure of the tip vortex still remains well-defined, and disconnected from the vortex sheets. Then, after one rotor revolution (Positions 21 and 22), the vortex structure interacts with the shear layer, before completely disappearing. The location of the maximum vorticity determines the centre of the CCW vortex. One can notice in Table 5, that the value of the maximum value of simple averaged vorticity decreases as the age of the vortex grows.

| Position | $(\omega_z)_{\max}$ ( $s^{-1}$ ) |
|----------|----------------------------------|
| 17       | 8055                             |
| 18       | 5288                             |
| 19       | 2015                             |
| 21       | 1196                             |

Table 5: Evolution of maximum of vorticity, along  $y_{hub}/R=0.70$  trajectory, for the MN configuration.

As mentioned before, the accuracy of the vorticity disk method depends on the number of common windows, which are contained in the smallest global window obtained by the conditional average procedure. The distributions of the number of common windows for Position 17 (beginning of trajectory), and Position 21 (end of trajectory), as well as the trace of the circle where the vorticity disk method is applied are plotted in Fig. 13.

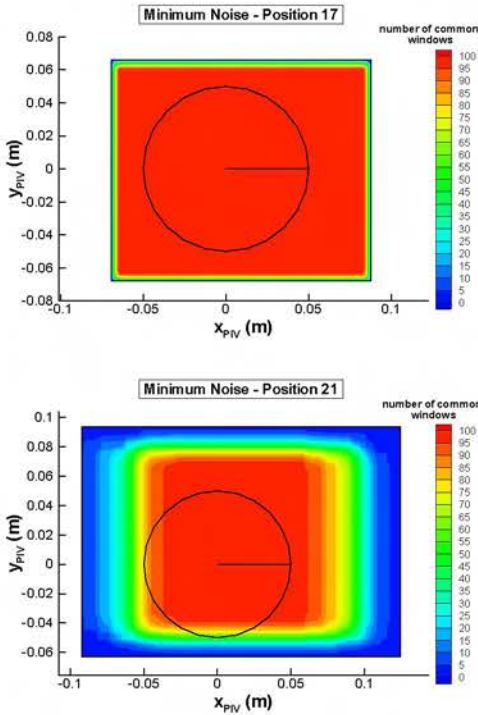


Figure 13: Distribution of common PIV windows on the smallest global window.

For the first position (Position 17), the integration circle contains all the 100 instantaneous shifted windows. This will provide a good accuracy of the vortex parameters. For the next to last position on the trajectory (Position 21), the integration circle covers areas where the number of common windows is decreased from 100 to 80. The vorticity disk method can still be applied, but a less accurate determination of the vortex parameters is expected. Figure 14 shows the radial evolutions of the circulation  $\Gamma$ , and the swirl velocity  $V_c$ , for the different positions along the trajectory.

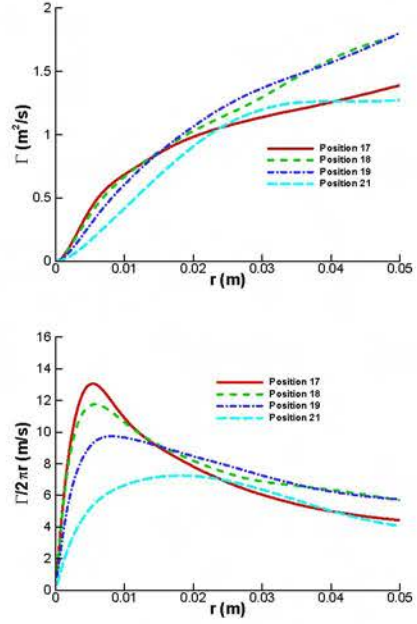


Figure 14: Radial evolution of circulation and swirl velocity, along  $y_{hub}/R=0.7$  trajectory, for the MN configuration.

One can notice a continuous evolution of the swirl distribution with respect to the age of the vortex, from Position 17 to Position 21. The peak of the swirl velocity is decreased, while the vortex core radius is increased. Table 6 summarizes the evolution of these values.

| Position | $\Gamma_c$ ( $m^2/s$ ) | $V_c$ (m/s) | $100r_c/c$ | n     |
|----------|------------------------|-------------|------------|-------|
| 17       | 0.451                  | 13.053      | 4.55       | 0.884 |
| 18       | 0.425                  | 11.754      | 4.76       | 0.686 |
| 19       | 0.505                  | 9.737       | 6.83       | 0.582 |
| 21       | 0.832                  | 7.254       | 15.10      | 0.420 |

Table 6: Vortex parameters along  $y_{hub}/R=0.70$  trajectory, for the MN configuration.

Furthermore, the swirl velocity distribution can be modelled by the Vatisas law (Refs. 8, 15), such as:

$$V(\rho) = \frac{\Gamma_c}{2\pi r_c} \cdot 2^{1/n} \cdot \frac{\rho}{(1 + \rho^{2n})^{1/n}}$$

where  $r_c$  is the vortex core size,  $\rho=r/r_c$ ,  $\Gamma_c$  is the circulation at  $r_c$ ,  $n=1$  corresponds to the Scully vortex model,  $n=\infty$  corresponds to the Rankine vortex model.

An iterative least square minimization method is applied to determine the variable n. The values of the n parameter obtained for each position are summarized in Table 6.

The comparisons between the experimental and theoretical (from Vatisas law) distributions of the swirl velocity are plotted in Fig. 15, for Position 17 and Position 21. It can be noted that the n values are determined to match in a satisfactory way within the vortex core (and less accurately outside of the core).

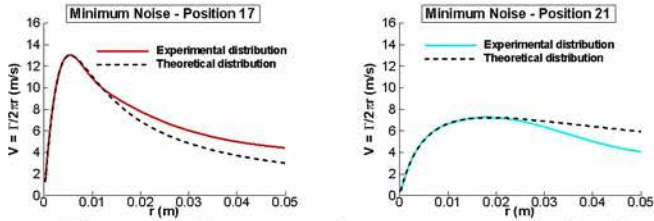


Figure 15: Comparison between experimental and theoretical swirl distribution, for Position 17 and 21 of the MN configuration.

### Comprehensive Analysis

The second part of the paper concerns the comparisons between the experimental data and the results of the ONERA aero-acoustic computational chain.

#### Computational Tools

The numerical methods used at ONERA are decomposed in five steps (Ref. 13). HOST (Ref. 17) is an aeroelastic code, developed by Eurocopter that trims the rotor taking into account aerodynamic, inertial and elastic forces and moments on the blades. The aerodynamic model is based on the lifting line method. In the METAR model (Ref. 18) the wake model is defined by a prescribed helicoidal geometry described by vortex lattices. A coupling between HOST and METAR is made until convergence is achieved on induced velocities at the rotor disk level, so that the rotor trim accounts for vortical wake and blade flexibility.

The prescribed wake geometry obtained by HOST/METAR is then distorted by using a free wake analysis code, MESIR (Ref. 19). In this code, a lifting line method similar to that in HOST/METAR is used. The blade motion calculated in HOST is given to the MESIR code. In the wake deformation process, the whole wake structure is distorted, and wake geometry iterations are continued until circulation convergence is achieved after a few iterations.

An intermediate step between wake geometry and blade pressure calculation is introduced using the MENTHE code (Ref. 20). During the roll-up process of the vortices, MENTHE identifies the portion of vortex sheets that the MESIR code calculated as having sufficiently strong intensity to roll-up. These rolled sheet regions constitute interacting vortices.

Blade pressure distribution is then calculated by the unsteady singularity method, ARHIS (Ref. 21). This code assumes that the flow around the rotor is inviscid and incompressible. It performs 2D-by-slices calculations. Subsonic compressibility effects are included by means of Prandtl-Glauert corrections combined with local thickening of the airfoil. In addition, finite span effects are

introduced through an elliptic-type correction of the pressure coefficients. The interacting vortices are modelled as freely convecting and deforming clouds of vortex elements. The main advantage of this method is the ability of taking into account the vortex deformation during strong blade-vortex interactions.

The noise radiation is computed by the PARIS code (Ref. 22), using pressure distribution calculated from ARHIS. The PARIS code is based on the Ffowcs Williams-Hawkings equation and predicts the loading and thickness noise. It uses a time domain formulation. An efficient spanwise interpolation method has been implemented, which identifies the BVI impulsive events on the signatures generated by each individual blade section.

#### Aerodynamic Analysis

Rotor trim. The rotor is trimmed to the experimental thrust and hub aerodynamic moments (equal to zero). Table 7 gives the experimental and computed values of control inputs. One can notice that the HOST calculations over-estimate by about  $1.7^\circ$  the collective pitch for the three configurations. This overestimation is related to the under-estimation of the mean value of elastic torsion deformation. The longitudinal cyclic pitch angle  $\theta_{1c}$  is under-estimated by about  $0.5^\circ$ , which could be due to the influence of the model support. The lateral cyclic pitch angle  $\theta_{1s}$  is rather well predicted (max of  $0.47^\circ$  of difference).

| Baseline                   | Experiment | Calculation |
|----------------------------|------------|-------------|
| $\theta_0$ ( $^\circ$ )    | 3.20       | 4.91        |
| $\theta_{1c}$ ( $^\circ$ ) | 2.00       | 1.41        |
| $\theta_{1s}$ ( $^\circ$ ) | -1.10      | -1.34       |

| Minimum Noise              | Experiment | Calculation |
|----------------------------|------------|-------------|
| $\theta_0$ ( $^\circ$ )    | 3.15       | 4.75        |
| $\theta_{1c}$ ( $^\circ$ ) | 2.04       | 1.55        |
| $\theta_{1s}$ ( $^\circ$ ) | -1.07      | -1.03       |

| Minimum Vibration          | Experiment | Calculation |
|----------------------------|------------|-------------|
| $\theta_0$ ( $^\circ$ )    | 3.16       | 4.99        |
| $\theta_{1c}$ ( $^\circ$ ) | 1.92       | 1.45        |
| $\theta_{1s}$ ( $^\circ$ ) | -1.11      | -1.58       |

Table 7: Comparison between experimental and predicted pitch angles.

Blade deflections. The blade deflections were measured optically by Stereo Pattern Recognition technique (SPR). Fig. 16 shows the azimuthal evolutions of the elastic flap ( $z_{el}$ ), the elastic lead-lag ( $y_{el}$ ), the elastic torsion ( $\theta_{el}$ ), and the total pitch angle ( $\theta_{tot} = \text{twist} + \text{pitch angle} + \text{elastic torsion}$ ) at the blade tip, for the three configurations. The flap deflection does not include the precone angle, and

is defined positive up. The lead-lag deflection is positive towards the leading-edge. The elastic torsion does not include the pitch control and the pre-twist, and is positive for the leading edge up.

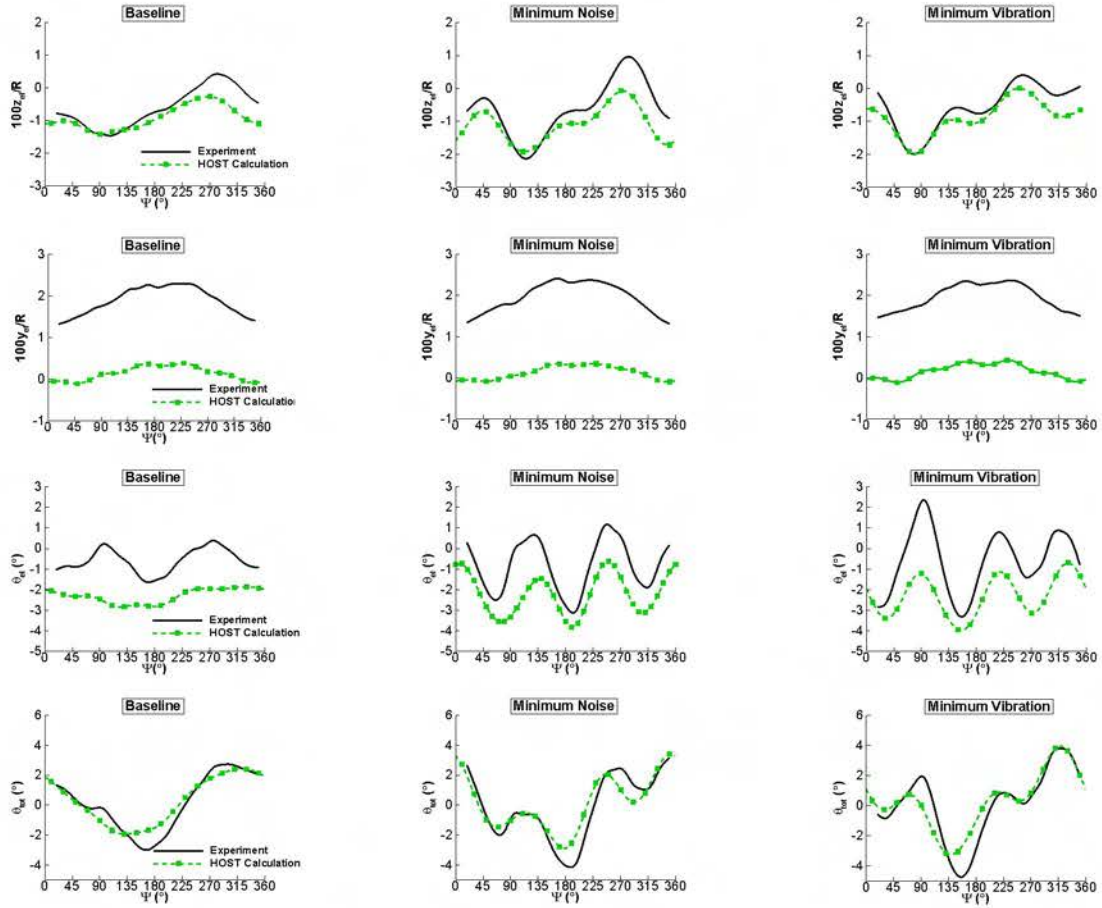


Figure 16: Azimuthal evolutions of the flap, lead-lag, elastic torsion and total pitch angle at the blade tip, for the BL, MN and MV configurations.

Generally speaking, rather satisfactory correlations are obtained between the experimental and computed blade tip deflections, for the three configurations.

For the Baseline configuration, a good 1/rev response of the flap and the lead-lag deflections, as well as of the total pitch angle is obtained. One can nevertheless notice that the 2/rev response of the elastic torsion is under-predicted. Furthermore, an offset of the static value of the elastic torsion is obtained, which is compensated by the larger predicted collective pitch angle to ensure the correct rotor thrust coefficient.

For the HHC cases (Minimum Noise and Minimum Vibration), strong 3/rev responses are well predicted by the HOST computations. An under-estimation of about  $1^{\circ}$  on the amplitude of the elastic torsion for these cases can also be noticed. Finally, an unexplained constant offset of the static value of the lead-lag deflection (equal to  $0.25c$ ) is observed for the three configurations.

#### Wake geometry.

The post-processing of the PIV data, described in the first part of the paper, provided the locations of the vortex centres (most of them being detected at the maximum value of vorticity on the advancing side, and at the minimum value of vorticity on the retreating side), in the PIV coordinate system. These coordinates are then transformed into the hub coordinate system, in order to be compared with the MESIR/MENTHE vortex locations, which were obtained by pre-test computations. The z-axis is defined positive up along the shaft axis. Fig. 17 shows top views of the wake geometry for the three configurations, and for the two azimuthal locations of the blade reference. Generally speaking, satisfactory correlations of the wake position in the top view are obtained for the three cases. More precisely, in the first quadrant (advancing side,  $\Psi=20^{\circ}$ ), the geometry of the tip vortex is well predicted for the Baseline case. For the Minimum Noise case, one can notice a difference between the experimental and predicted orientations of the lattices, in the first quadrant ( $\Psi=20^{\circ}$ , advancing

side), in the azimuthal area where the interactions occur. The consequence of this difference will be shown in the acoustic analysis. For the MV case, the predicted locations of the CCW inboard vortices are slightly too much upstream, in the first quadrant. In the second quadrant (advancing side,  $\Psi=70^\circ$ ), the predicted locations of the centres of the tip vortex for the BL and MN cases, and of the inboard vortex for the MV case, are slightly too much inboard. In the third quadrant (retreating side,  $\Psi=20^\circ$ ), correlations with experiment are very satisfactory. In the fourth quadrant (retreating side,  $\Psi=70^\circ$ ), the predicted locations of the centres of the tip vortex are slightly too much upstream. Furthermore, for the Minimum Vibration configuration, the predictions of the locations of the centres of the tip vortex on the advancing side of the blade ( $\Psi=20^\circ$  and  $\Psi=70^\circ$ ) are very satisfactory. Figure 18 shows the side view of the wake geometry for the three configurations, in the advancing and retreating sides, for the lateral planes at  $y_{hub}=\pm 1.4m$ . Generally speaking, the predicted locations of the vortex centres on the advancing side are below the experimental data, of about 0.5 chord for BL, 0.3 chord for MN, and up to 0.5 chord for MV. On the retreating side, the predictions in the fourth quadrant ( $\Psi=70^\circ$ ) are satisfactory, while they are still located below the experimental points in the third quadrant ( $\Psi=20^\circ$ ), by about 0.3 chord. These discrepancies could come from the lifting line modelling, which could generate shifted locations where the vortices are

emitted (the chord dimension being not taken into account).

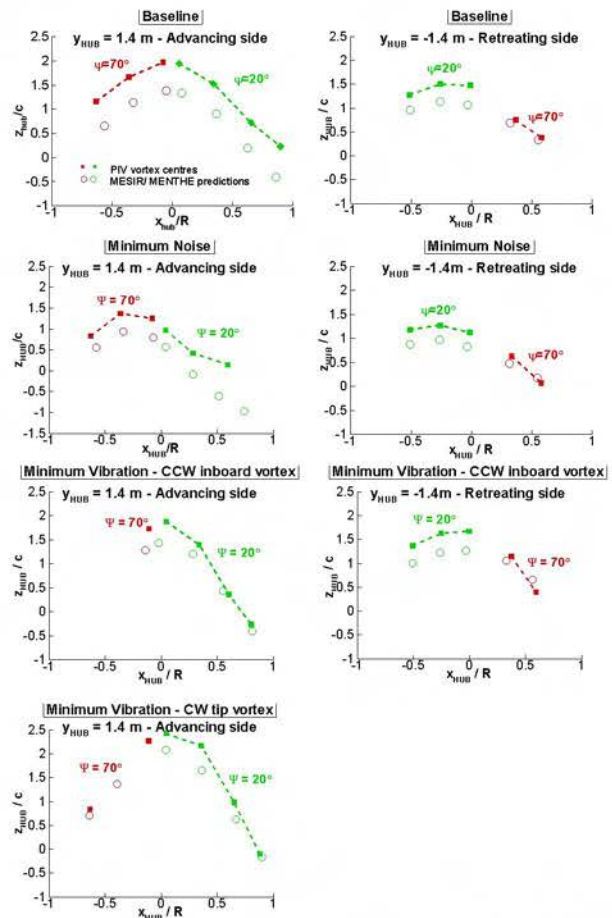


Figure 18: Comparison between experimental and predicted wake geometries on side view, for the BL, MN and MV configurations.

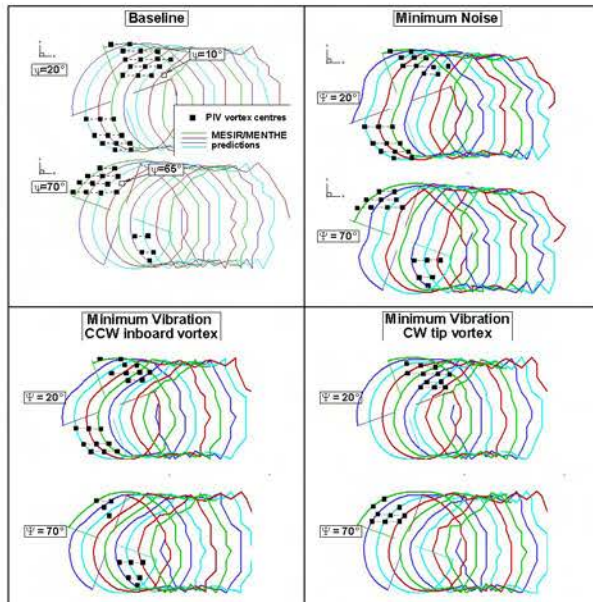


Figure 17: Comparison between experimental and predicted wake geometries on top view, for the BL, MN and MV configurations.

### Acoustic Analysis

The acoustic results are first presented in terms of noise contours plotted on a plane located 2.25m below the rotor. In the experiment, an array of 13 microphones is moved in the streamwise direction and data points are recorded every 0.5m. The noise levels are filtered in the range of 6 to 40 times the blade passage frequency which is known to be the frequency range where BVI noise is dominant. The comparison of experimental and calculated noise contour levels is shown in Figure 19 for the BL, MN and MV cases. The experimental results show, like during the HART tests, that the maximum level is lower in the MN case than in the BL case and that the directivity is shifted in front of the rotor. For the MV case, the maximum level is increased and the directivity pattern is similar to the BL case. The agreement between calculations and experiment can be considered as quite good. In particular, the noise reductions in the MN case and, on the contrary, the noise increase in the MV case are well predicted.

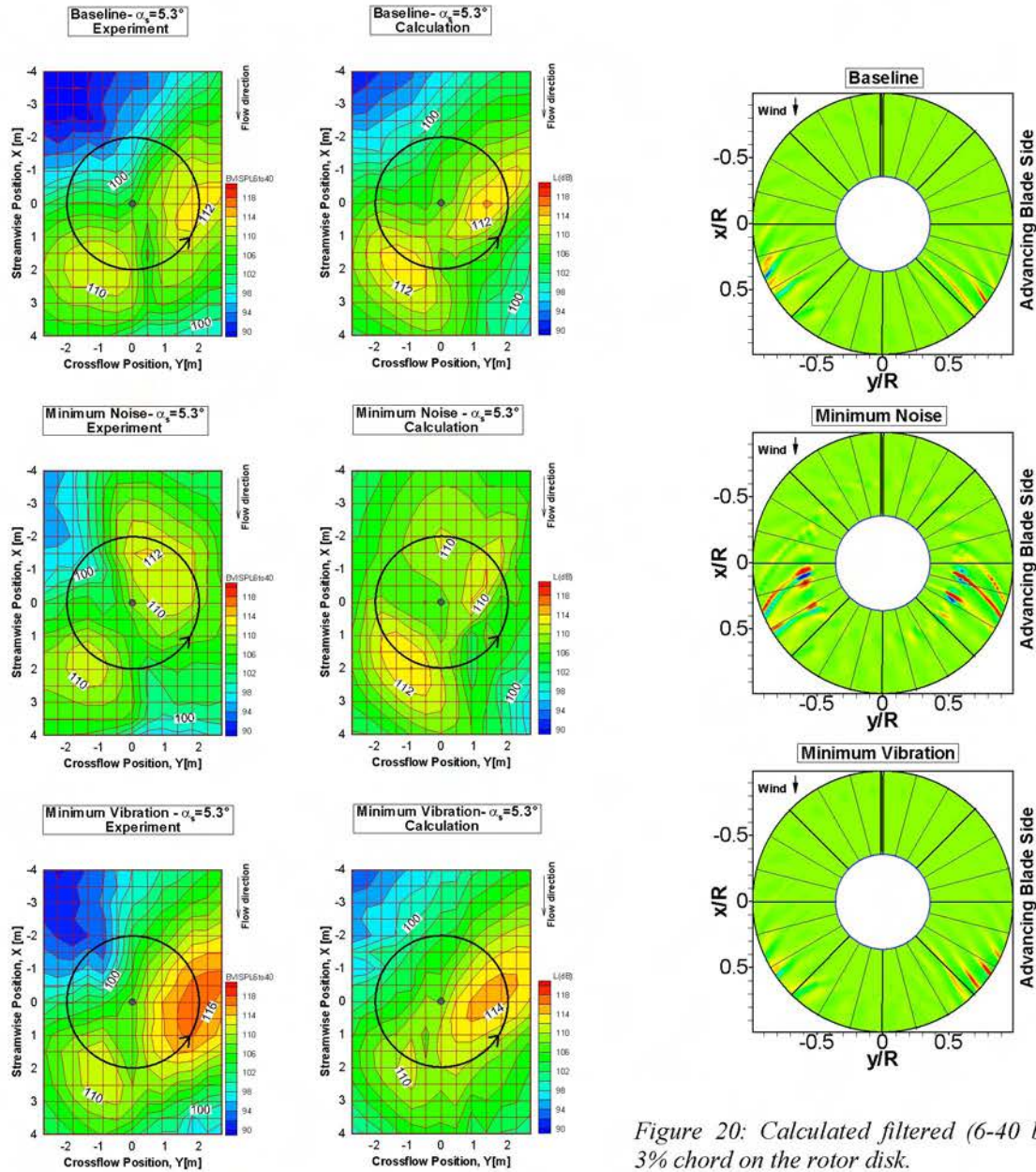


Figure 19: Comparison between experimental and predicted noise contour levels for the BL, MN and MV configurations.

The directivity patterns give an indication of the location of the vortices when they interact with the blades. Directivity more in front of the rotor like in the MN case indicates that the interactions occur at higher azimuths, which happens when the wake is convected faster below the rotor plane. The vortex centre positions shown on Figs. 17 and 18 are in agreement with this analysis. The plotting of the calculated  $\Delta C_p$  at 3% chord (Figure 20) confirms that the interactions occur at higher azimuths for the MN case (at  $45^\circ$  and  $55^\circ$  for the BL case,  $65^\circ$  for the MN). For the MV case, four interactions seem to be able to generate noise in the blade tip area.

Figure 20: Calculated filtered (6-40 bpf)  $\Delta C_p$  at 3% chord on the rotor disk.

To complete this first analysis, we have plotted on Figure 21 the sectional loads histories and the corresponding azimuthal derivatives at  $r/R=0.87$  computed by the aerodynamic code ARHIS (which performs a calculation with a sufficiently small azimuthal step). Good correlations with experiment are obtained, in terms of strong fluctuations around  $60^\circ$  on the advancing side, and  $300^\circ$  on the retreating side (characteristic of BVI noise occurrence). The amplitude and phase of the peaks appearing on the  $d(C_n M^2)/d\psi$  coefficients on the advancing blade side are generally fairly well predicted. Note that in the MN case no interaction occurs before  $\psi=70^\circ$ .

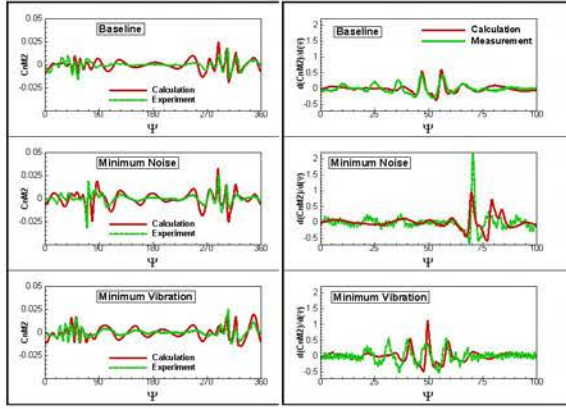


Figure 21: Comparison between experimental and predicted sectional loads (left) and azimuthal derivatives (right) at  $r/R=0.87$ , low-pass filtered (up to 8/rev).

Nevertheless, the examination of the azimuthal derivatives of the  $CnM^2$  coefficients and the  $\Delta C_p$  is not sufficient to predict the number and the strength of the actual acoustic pressure peaks. Indeed, strong blade pressure fluctuations do not automatically result in high acoustic levels. For example, in the MN case, the interaction occurs at a blade azimuth too large to produce high BVI level despite a strong pressure peak.

The noise contours also do not clearly reveal the number of interactions. Only the acoustic time signatures can provide this information. They are plotted on Figure 22 for the microphone located at the measured or calculated maximum noise level. For the BL case, the acoustic peak is overestimated by 1.3dB by the computation. It has been checked that this is because the predicted blade vortex miss-distances are smaller than the experimental ones. In the MN case, the peaks are fairly well predicted (when neglecting the low frequency part of the signal) even if the directivity pattern shown on the contour plots is a little bit different. This disagreement is caused by the difference of orientation of the predicted and measured vortices as shown on Figure 17.

It clearly appears that for the MV case, a succession of several interactions contribute to the total noise contrarily to the BL case where only one strong interaction occurs even if the directivities of the contour plots are very similar. In the MV case, the calculated peaks are in good agreement with measurements both in terms of amplitude and number of peaks as shown on the detailed view of Figure 23. The noise level is higher in the experiment because the strongest interaction is closer to the blade than in the calculation.

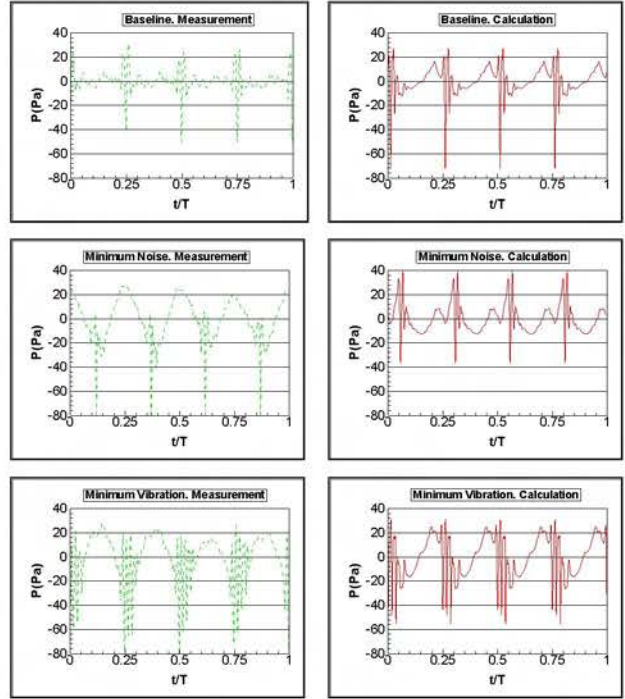


Figure 22: Comparison between experimental and predicted time signatures at maximum noise location, for the BL, MN and MV configurations.

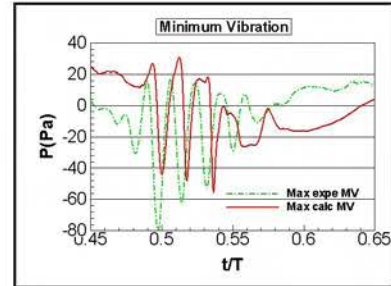


Figure 23: Comparison between experimental and predicted time signatures at maximum noise, for the MV configuration.

The calculated blade vortex miss-distances presented on Figure 24 explain the differences of the acoustic results between the three HHC cases. In the MN case, the vortices are much lower, as expected from the previous results. In the MV case, compared to the BL case, the vortices are less parallel to the blade in the vertical direction. As a consequence, more vortices are close to the blade tip. This explains the numerous BVI peaks measured and calculated on the advancing blade side.

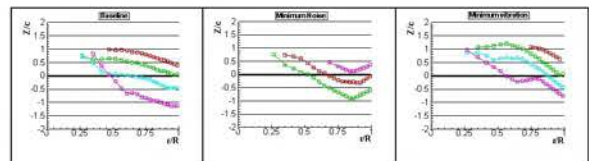


Figure 24: Blade vortex miss-distances at the azimuths of interaction for the BL, MN and MV configurations.

### Concluding remarks

The 3C PIV database from the HART II campaign provides very interesting and detailed information on the flowfield (and more especially on wake geometry) for a rotor in descent flight, piloted with different pitch control laws. Different analyses have been performed to:

- understand the influence of the pitch control laws on the convection and interactions of the vortices with the blade (responsible for BVI noise);
- determine the vortex parameters, such as swirl velocity distribution and vortex core size.

These experimental data will be compared to the predicted vortex parameters in a future study.

These data should also be used to evaluate and improve the vortex model and the predictions of the wake geometry by free-wake methods or CFD codes.

On the other hand, comparisons between experiment and the ONERA aero-acoustic computational chain have been performed. The results of the different steps of this methodology have been carefully analysed:

- lift predictions are satisfactory. The strong BVI phenomenon for the Baseline configuration is well predicted;
- blade tip deformations are rather well predicted. The stronger 3/rev responses for the HHC cases are obtained. Nevertheless, an under-estimation of the amplitude of the elastic torsion is obtained;
- the predictions of the wake geometries on top view are rather good, despite a slightly too much inboard locations of the vortices in the first quadrant;
- the comparisons of noise radiation are satisfactory, in terms of noise levels and directivity.

Improvements of the free wake model in the ONERA computational chain have already been undertaken. A new free wake model, featuring as a fully unsteady time-marching method, begins to be validated for BVI noise prediction for unsteady flight manoeuvres (Ref. 23). The use of curved lifting-line theory, which is able to take into account non-conventional blade planforms, could also give improved results. In a longer term, one can expect to use directly CFD methods to capture the blade-vortex interactions, but significant efforts must be done to reduce the diffusion of these methods (use of higher order schemes, and adaptive grids).

### Acknowledgments

The authors would like to acknowledge all the participants to the HART and HART II campaigns, and more especially B. van der Wall from DLR, C. Burley from NASA Langley, J. Lim from AFDD, and K. Pengel from DNW, without whom all these fruitful data would not be available.

### References

1. Yu, Y.H., Gmelin, B., Heller, H., Philippe, J.J., Mercker, E., Preisser, J.S., "HHC Aeroacoustic Rotor Test at the DNW – the Joint German/French/US HART Project", 20<sup>th</sup> European Rotorcraft Forum, Amsterdam, Netherlands, 1994.
2. Spletstoesser, W.R., Kube, R., Wagner, W., Seelhorst, U., Boutier, A., Micheli, F., Mercker, E., Pengel, K., "Key results from a Higher Harmonic Control Aeroacoustic Rotor Test (HART)", Journal of the American Helicopter Society, January 1997.
3. Yu, Y.H., Tung, C., van der Wall, B.G., Pausder, J., Burley, C. L., Brooks, T., Beaumier, P., Delrieux, Y., Mercker, E., Pengel, K., "The HART-II Test: Rotor Wakes and Aeroacoustics with Higher-Harmonic Pitch Control (HHC) Inputs – The Joint German/French/Dutch/US Project", American Helicopter Society 58<sup>th</sup> Annual Forum, Montreal, Canada, May 2002.
4. Richard, H., Raffel, M., "Rotor Wake Measurements: Full-Scale and Model Tests", American Helicopter Society, 58<sup>th</sup> Annual Forum, Montreal, Canada, May 2002.
5. van der Wall, B.G., Junker, B., Burley, C.L., Brooks, T., Yu, Y.H., Tung, C., Raffel, M., Richard, H., Wagner, W., Mercker, E., Pengel, K., Holthusen, H., Beaumier, P., Prieur, J., "The HART-II Test in the LLF of the DNW – a Major Step towards Rotor Wake Understanding", 28<sup>th</sup> European Rotorcraft Forum, Bristol England, September 2002.
6. Pengel, K., Mueller, R., van der Wall, B.G., "Stereo Pattern Recognition – the technique for reliable rotor blade deformation and twist measurement", Heli-Japan 2002, AHS International Meeting on Advanced Rotorcraft Technology and Life Saving Activities, Utsunomiya, Japan, November 2002.
7. Lim, J.W., Tung, C., Yu, Y.H., Burley, C.L., Brooks, T., Boyd, D., van der Wall, B.G., Raffel, M., Beaumier, P., Bailly, J., Delrieux, Y., Pengel, K., Mercker, E., "HART II – Prediction of Blade-Vortex Interaction Loading", 29<sup>th</sup> European Rotorcraft Forum, Friedrichshafen, Germany, September 2003.

8. Burley, C., Brooks, T.F., van der Wall, B.G., Richard, H., Raffel, M., Beaumier, P., Lim, J.W., Yu, Y.H., Tung, C., Pengel, K., "Rotor Wake Vortex Definition and Validation from 3-C PIV HART-II Study", 28<sup>th</sup> European Rotorcraft Forum, Bristol, England, September 2002.
9. Yu, Y.H., Tung, C., van der Wall, B.G., Pausder, H., Burley, C.L., Brooks, T., Beaumier, P., Delrieux, Y., Mercker, E., Pengel, K., "The HART – II Test: Rotor Wakes and Aeroacoustics with Higher-Harmonic Pitch Control (HHC) Inputs – The Joint German/French/Dutch/US Project", American Helicopter Society 58<sup>th</sup> Annual Forum, Montreal, Canada, June 2002.
10. Tung, C., Gallman, J.M., Kube, R., Wagner, W., van der Wall, B.G., Brooks, T., Burley, C.L., Boyd, D.D., Rahier, G., Beaumier, P., "Prediction and Measurement of Blade-Vortex Interaction Loading", 1<sup>st</sup> Joint CEAS/AIAA Aeroacoustics Conference, Munich, Germany, June 1995.
11. Beaumier, P., Spiegel, P., "Validation of ONERA Aeroacoustic Prediction Methods for Blade-Vortex Interaction using HART Tests Results", 51<sup>st</sup> Annual Forum and Technology Display, AHS, Fort Worth, May 1995.
12. Raffel, M., Richard, H., Schneider, G., Klinge, F., Ehrenfried, K., Pengel, K., Geenstra, G., "Recording and Evaluation Methods of PIV Investigations on a Helicopter Rotor Model", 11<sup>th</sup> International Symposium on Applications of Laser Techniques to Fluid Mechanics, Lisbon, July 2002.
13. Beaumier, P., Delrieux, Y., "Description and Validation of the ONERA Computational Method for the Prediction of Blade-Vortex Interaction Noise", 29<sup>th</sup> European Rotorcraft Forum, Friedrichshafen, Germany, September 2003.
14. Jeong, J., Hussain, F., "On the Identification of a Vortex", *Journal of Fluid Mechanics*, vol. 285 – pp. 69-94, 1995.
15. Batchelor, G.K., "An Introduction to Fluid Dynamics", Cambridge University Press, 1967, pp 84-108.
16. Vattistas, G.H., Kozel, V., Mih, W.C., "A Simpler Model for Concentrated Vortices", *Experiments in Fluids*, vol. 11, 1991.
17. Benoit, B., Dequin, A.M., Kampa, K., Grunhagen, W., Basset, P.M., Gimonet, B., "HOST, a General Helicopter Simulation Tool for Germany and France", 56<sup>th</sup> Annual Forum of the American Helicopter Society, Virginia Beach, VA, May 2002.
18. Arnaud, G., Beaumier, P., "Validation of R85/METAR on the Puma RAE flight tests", 18<sup>th</sup> European Rotorcraft Forum, Avignon, France, September 1992.
19. Michéa, B., Desopper, A., Costes, M., "Aerodynamic Rotor Loads Prediction Method with Free Wake for Low Speed Descent Flight", 18<sup>th</sup> European Rotorcraft Forum, Avignon, France, September 1992.
20. Rahier, G., Delrieux, Y., "Improvement of Helicopter Rotor Blade-Vortex Interaction Noise Prediction using a Rotor Wake Roll-Up Model", 16<sup>th</sup> AIAA Aeroacoustic Conference, Munich, Germany, June 1995.
21. Spiegel, P., Rahier, G., Michéa, B., "Blade-Vortex Interaction Noise: Prediction and Comparison with Flight and Wind Tunnel Tests", 18<sup>th</sup> European Rotorcraft Forum, Avignon, France, September 1992.
22. Spiegel, P., Rahier, G., "Theoretical Study and Prediction of BVI Noise Including Close Interactions", AHS Technical Specialists Meeting on Rotorcraft Acoustics and Fluid Mechanics, Philadelphia, PA, October 1991.
23. Pérez, G., Costes, M., "A New Aerodynamic and Acoustic Computation Chain for BVI Noise Prediction in Unsteady Flight Conditions", 60<sup>th</sup> Annual Forum of the American Helicopter Society, Baltimore, USA, June 2004.